Inorganic Chemistry

Article

pubs.acs.org/IC

Synthesis and Characterization of a Novel Sodium Transition Metal Oxyfluoride: $NaMnMoO_3F_3·H_2O$

Jessica Nava-Avendaño,[†] Carlos Frontera,[†] José A. Ayllón,[‡] Judith Oró-Solé,[†] Premkumar Senguttuvan,[†,§] and M. Rosa Palacín*[,†]

[†]Institut de Ciència de Materials de Barcelona (ICMAB-CSIC), ALISTORE-ERI European Research Institute, Campus UAB, E-08193 Bellaterra, Catalonia, Spain

[‡]Departament de Química, Universitat Autònoma de Barcelona, Campus UAB, E-08193 Bellaterra, Catalonia, Spain

[§]Laboratoire de Réactivité et Chimie des Solides, ALISTORE-ERI European Research Institute, UPJV, CNRS UMR6007, 33 rue Saint Leu 80039 Amiens, France

Supporting Information

ABSTRACT: $NaMnMoO_3F_3·H_2O$ was precipitated at low temperature from aqueous dissolutions of $Na_2MoO_4·2H_2O$ in aqueous HF (or $NaHF_2$) using either $Mn(CH_3COO)_2·4H_2O$ or MnF_2 as manganese precursors. Chemical analysis, IR spectra, and effective paramagnetic moment are in agreement with the proposed formula. Electron microscopy studies indicate that the sample is constituted of very thin plate-like microcrystals. The average crystal structure (a = 3.5947(1), b = 21.246(1), and c = 7.3893(2) Å and $Cmcm$ (No. 63) SG) has been elucidated through powder diffraction methods (synchrotron and neutron). Tiny superstructure peaks are observed that can be indexed with the space group $Pbca$ and cell parameters a = 7.1894(2), b = 21.246(1), and c = 7.3893(2) Å. Electron diffraction confirms the doubling of a parameter. Ordering of O and F is proposed in agreement with Pauling's second crystal rule and bond strength sums for each anionic position. The structure that is formed has a layered stacking arrangement along the b-axis of the MnO_4F_2 octahedra layers that share corners along a- and c-directions. The large interlayer space contains MoO_4F_2 octahedra (connected to the layer) together with sodium ions and water molecules, tentatively forming hydrogen bonding with fluorine anions. The origin of the superstructure could not be fully elucidated, but it is presumably related to slight distortions within the MnO_4F_2 octahedra.

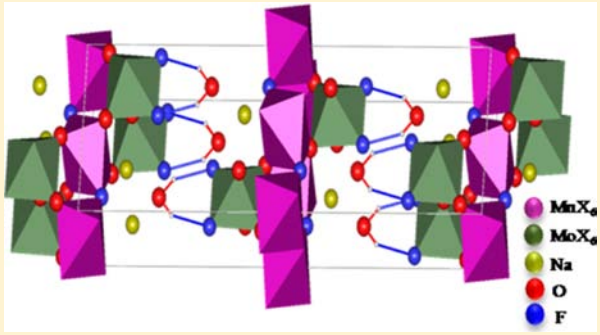

INTRODUCTION

Fluorides are key in some applications such as nuclear energy (e.g., uranium hexafluoride in isotopic separation plants) or in metallurgy (aluminum fluoride or cryolite, Na_3AlF_6 in aluminum production and refining, calcium fluoride in steel elaboration, and others)[1] and, therefore, have attracted the sustained attention of scientists. Further, the interest in oxyfluorides arose as the physical properties of materials are usually modified by oxygen−fluorine replacement, as a consequence of the similar size of the isoelectronic O^{2-} and F^- anions.[2] Indeed, this substitution takes place in structural types as diverse as rutile, perovskite, and garnet, among others, and the charge is compensated either by reduction of the metal oxidation state (e.g., for transition metals) or by appropriate cationic balancing through aliovalent substitutions. A striking example of the effect of the oxygen−fluorine exchange is the decrease in the Curie temperature for ferroelectric oxides due to the smaller covalency of the M−F bonds.[3] Aside from such considerations, the study of anion ordering in oxyfluorides is intrinsically challenging for the inorganic chemist due to the similar ionic radius and both the X-ray and neutron diffraction scattering factors for both anions. In spite of some very relevant predictive approaches,[4] a posteriori quantification is a regular practice to determine the reliability of a determined proposed order or disorder scheme.

Fluorine-containing phases have also been proposed as electrode materials for secondary lithium batteries.[5] Indeed, materials operating through conventional insertion[6,7] or alternative conversion-type[8,9] mechanisms are presently enjoying the arrival of fluorinated compounds. The advantages of fluorinated phases stem from the higher electronegativity of the M−F bond that leads to higher ionicity and, hence, higher redox potentials when used as electrode materials, while their drawbacks are usually related to their highly insulating character. Yet, promising results have been reported through electrode processing involving the formation of nanocomposites with carbon and binary[10] or ternary fluorides[11,12] not only for lithium ion batteries but also for the analogous emerging sodium ion battery technology.[13,14] Alternatively, silver

Received: March 7, 2013
Published: August 9, 2013

   dx.doi.org/10.1021/ic401447p | Inorg. Chem. 2013, 52, 9791−9797

vanadium oxyfluorides have been proposed as high-capacity positive electrode materials for primary cells in high-rate applications such as implantable cardioverter defibrillators.[15,16]

In light of such scenarios, we decided to investigate mixed sodium transition metal fluorides and oxyfluorides with special emphasis on metals with rich redox chemistry. The recent report about the synthesis of $CsMnMoO_3F_3$[17] prompted us to investigate phases in the Na−Mn−Mo−O−F system. Although statistical disorder for Mn(II)/Mo(VI) and also O/F anions was found in the three-dimensional $CsMnMoO_3F_3$ structure, the much smaller ionic radius for sodium, when compared to cesium,[2] allows us to envision that a different structural type would form with reasonably lower coordination number (CN) for sodium ions[18] (note that the CN of cesium ions in $CsMnMoO_3F_3$ is 18).

EXPERIMENTAL SECTION

Materials. Aqueous HF (48%, Aldrich), $Na_2MoO_4{\cdot}2H_2O$ (Aldrich), MnF_2 (98%, Aldrich), $Mn(CH_3COO)_2{\cdot}4H_2O$ (Aldrich), and $NaHF_2$ (granular, 98%, Aldrich) were used. All precursors were used without further purification.

Caution: hydrofluoric acid is highly corrosive and irritating. Its use requires extreme caution, and it must be handled with protective clothing. Specialized treatment is required in case of contact with liquid or vapor HF.[19,20]

Synthesis. $NaMnMoO_3F_3{\cdot}H_2O$ was obtained by three slightly different synthetic routes using $Na_2MoO_4{\cdot}2H_2O$ as the molybdenum source. All syntheses were carried out in polypropylene beakers. The precursors were dissolved in distilled water, were mixed together, and were brought to dryness on a hot plate at 80 °C. *Route 1* (45% yield) involved mixing a 0.726 g (3.00×10^{-3} mol) solution of $Na_2MoO_4{\cdot}2H_2O$ (≈0.12 M) with a 0.496 g (8.00×10^{-3} mol) solution of $NaHF_2$ (≈0.32 M) and 0.279 g (3.00×10^{-3} mol) of MnF_2. Distilled water was added until a final volume of 80 mL was reached. After magnetic stirring and sonication, a small amount of undissolved material was separated by centrifugation, and the remaining clear material was then brought to dryness. The solid remainder was repeatedly washed with water and finally dried at 60 °C in air. The other two routes involved the use of $Mn(CH_3COO)_2{\cdot}4H_2O$, as a manganese precursor, and HF, and the two routes differed only in the overall sodium concentration in the reacting mixture. *Route 2* (25% yield) consisted of mixing a 7.26 g (3.0×10^{-2} mol) solution of $Na_2MoO_4{\cdot}2H_2O$ (≈0.6 M) with a 7.35 g (3.0×10^{-2} mol) solution of $Mn(CH_3COO)_2{\cdot}4H_2O$ (≈0.6 M), a 4.62 g (11.0×10^{-2} mol) solution of NaF (≈4.4 M), and finally a 4 mL solution of HF (48% aqueous solution, 9.6×10^{-2} mol). The larger sodium concentration resulted in the direct precipitation of $NaMnF_3$, which was subsequently separated by decantation. The remaining solution was treated following the procedure described above. Finally, *Route 3* (60% yield) allowed us to avoid the formation of any byproduct in the course of the reaction starting from a 2.41 g (1.00×10^{-2} mol) solution of $Na_2MoO_4{\cdot}2H_2O$ (≈0.2 M) with a 2.45 g (1.00×10^{-2} mol) solution of $Mn(CH_3COO)_2{\cdot}4H_2O$ (≈0.2 M) and 1.5 mL of HF (48%, aqueous solution, 4.08×10^{-2} mol), which yielded a clear solution after mixing. In this case, the mixture was also heated at 80 °C but not brought to dryness. The precipitated solid was recovered after 10 h of reaction, and it was washed and dried, as in the other two cases. The XRPD pattern was identical for all samples, except for the presence of a tiny amount of unidentified impurities on the large batch prepared for neutron diffraction. Attempts to obtain single crystals that were carried out at 150 °C under hydrothermal conditions were all unsuccessful, yielding mixtures of manganese fluoride and molybdenum oxide.

Dissolution of the sample for chemical analysis was done through digestion with ≈40 mg of an as-prepared solid sample in a mixture of HNO_3 (Baker Instra), H_2O_2 (Merck Suprapur), and HF (Scharlau) inside a closed Teflon reactor in a microwave furnace at 200 °C. Manganese and molybdenum content was determined by ICP-OES using a Perkin-Elmer Optima 3200 RL, and sodium content was determined through ICP-MS using a Perkin-Elmer Elan 6000 spectrometer.

The IR spectrum (500−4000 cm^{-1}) was collected using a Perkin-Elmer FT-IR Spectrum One system with a universal attenuated transmission reflectance (ATR) accessory and a DiComp crystal composed of a diamond ATR with a ZnSe focusing element.

Scanning electron microscopy (SEM) was carried out using a field-emission gun microscope (Quanta 200 ESEM FEG FEI) that was equipped with an energy-dispersive X-ray spectrometer (EDX). Transmission electron microscopy (TEM) and electron diffraction (ED) were performed on a JEOL 1210 transmission electron microscope operating at 120 kV and equipped with a Gathan sample holder allowing ±60° x and ±30° y-tilting. Preparation of the samples involved dispersing the powder in heptane (anhydrous, 99%) and depositing a droplet of the dispersion on a holey carbon-coated copper grid.

The X-ray powder diffraction (XRPD) on as-prepared samples has been carried out using a Siemens D-5000 diffractometer (Cu Kα radiation) in the 2θ range of 5−80° with a 2θ step size of 0.02°. Two different sample holders were used for XRPD measurements: a standard one in which the material is pressed from the top to get a flat surface and a second one that is side-loaded. Additional high-resolution synchrotron powder diffraction patterns were collected at the 11-BM beamline (λ = 0.413548 Å) of the Advanced Photon Source (Argonne National Lab, mail-in program) using 0.5 mm diameter borosilicate capillaries, which were rotated during data collection. Neutron powder diffraction (NPD) pattern at RT was measured at D2B beamline at the Institut Laue Langevin (Grenoble, France, EASY access system)[21] in the high-flux mode (λ = 1.594 Å) with Debye−Scherrer geometry using ≈2 g of sample placed inside an ≈8 mm diameter vanadium sample holder. DICVOL,[22] DAJUST,[23] XLENS,[24] and FullProf_suite[25] programs were used for indexing the patterns, intensity extraction, resolution of the structure, and structure completion/refinement, respectively.

Magnetization has been measured using a superconducting quantum interferometer device (SQUID, Quantum Design). Measurements were done with an applied field of 1000 Oe upon heating after a field-cooling process from 10 to 350 K.

Electrochemical tests were performed in two-electrode Swagelok cells using a sodium metal cube slice (Aldrich 99.95%) as the counter electrode. Two sheets of Whatman GF/D borosilicate glass fibers were used as separators; they were soaked with 1 M $NaClO_4$ in a 50/50 (wt %) mixture of propylene carbonate (PC) and ethylene carbonate (EC). The cells were tested using a MacPile potentiostat (Bio-Logic, France). The working electrode consisted of ≈5−6 mg of a powder mixture of the active material ball-milled for 12 h with 40% of carbon black (Super P, Timcal, Switzerland). The performance was evaluated through galvanostatic cycling with potential limitation (GCPL) experiments at the $C/25$ rate.

RESULTS AND DISCUSSION

XRPD pattern, typical SEM micrographs, and the IR spectrum for $NaMnMoO_3F_3{\cdot}H_2O$ are depicted in the Supporting Information (SI) and Figure 1a,b, respectively. They were the same in all cases, regardless of the minor differences in the synthetic routes. Significant preferred orientation has been detected by comparing XRPD patterns obtained using standard and side-loaded sample holders (Bragg−Bentano geometry).

Scanning electron microscopy revealed that the samples are constituted of very thin micrometric crystallites (Figure 1a), and EDX data allowed us to ascertain that the elemental composition is homogeneous, with an O/F ratio larger than 1. Chemical analysis yielded 7.8 (σ = 0.15), 17.4 (σ = 0.05) , and 33.2 (σ = 0.05) as weight % for sodium, manganese, and molybdenum, which are fully consistent with the expected values (7.74, 18.50, and 32.31) for $NaMnMoO_3F_3{\cdot}H_2O$.

The IR spectrum taken in ATR mode is depicted in Figure 1b. The bands at 1651, 3516, and 3563 cm^{-1} that correspond to

dx.doi.org/10.1021/ic401447p | Inorg. Chem. 2013, 52, 9791−9797

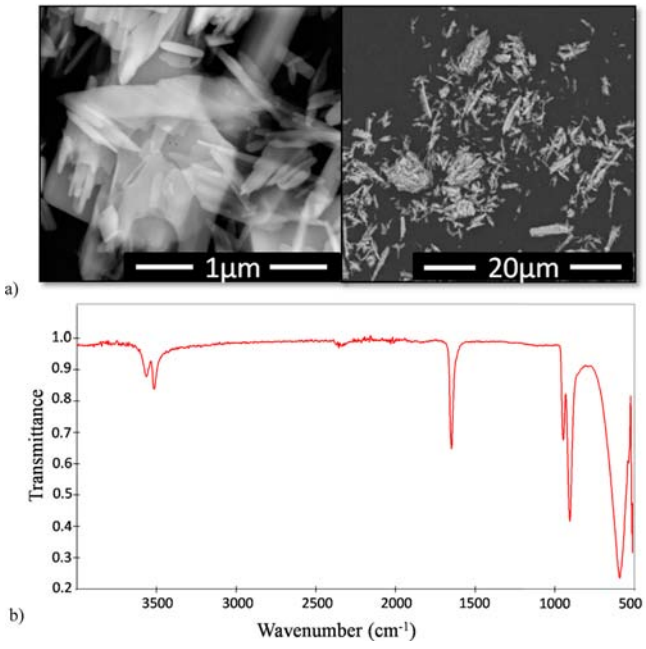

Figure 1. (a) SEM images at different magnifications for $NaMnMoO_3F_3{\cdot}H_2O$ and (b) ATR-IR spectrum of an as-prepared sample showing characteristic vibration bands of the water contained in the crystal lattice at 1651, 3516, and 3563 cm^{-1}.

the HOH bending and the O−H antisymmetric and symmetric stretching vibrations, respectively, clearly confirm the presence of water in the product. The absence of other bands in that region excludes the possibility of having major amounts of OH^- or H_3O^+ in the crystalline lattice.[26−28] The absorption bands observed in the range of 600−1000 cm^{-1} may be ascribed to M−O (M = Mo, Mn) (note that stretching vibrations for M−F bands would be expected at lower wavenumber).[29] The presence of water molecules is consistent with the synthesis method using low temperature and ambient pressure, and contrasts with other related compounds,[17,28−33] prepared under different conditions.

The DC magnetization and inverse susceptibility versus temperature are shown in Figure 2. The validity of the Curie−Weiss law in this compound is clear from the linear behavior of χ^{-1}. The effective paramagnetic moment extracted per Mn ion is μ_{eff} = 5.87(2) μ_B/Mn, assuming that the composition is $NaMnMoO_3F_3{\cdot}H_2O$. Such a result is fully consistent with the expected value for Mn(II) (5.92 μ_B/Mn) and the presence of diamagnetic Mo(VI), and hence, both metals remain in the same oxidation state as the precursors that were used for the synthesis.

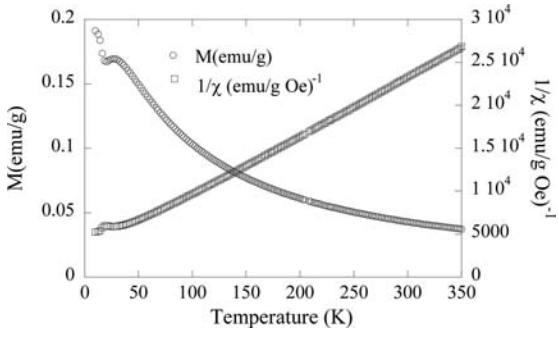

Figure 2. DC magnetization and inverse susceptibility obtained under a field of 1000 Oe and after a field-cooling process.

The laboratory XRPD pattern of the sample was different from the one exhibited by $CsMnMoO_3F_3$, which was expected due to both the smaller size of sodium with respect to cesium and also to the presence of crystallization water. The pattern was successfully indexed with an orthorhombic cell with parameters a = 3.595, b = 21.247, and c = 7.389 Å. Systematic reflection absences in these patterns indicate that the lattice is C-face centered, and according to SGAID tool (DAJUST program), the possible space groups (SG) are $Cmcm$, $Cmc2_1$, and $C2cm$. The indexing of the pattern provides evidence that the reflections that are enhanced due to the preferred orientation correspond to $0k0$-type, which is in agreement with the plate-like morphology of the crystallites. First attempts to solve the structure were conducted assuming a centrosymmetric $C\,mcm$ (No. 63) SG, but finding the location of water molecules was not possible. A peak in the real space electronic density was clearly found at the 4c Wyckoff position with y = 0.31, and a Na atom was initially placed at this position. Synchrotron XRPD patterns were satisfactorily indexed and refined using the structural model derived from laboratory XRPD, thus confirming its validity. The NPD pattern shows odd background noise, which is fully consistent with the presence of hydrogen atoms in the compounds. While the NPD pattern can be indexed with the cell parameters derived from the XRPD data, it cannot be successfully fitted with the proposed structural model. To understand this and to complete the structural elucidation, we first ran Patterson analyses with the extracted integrated intensities, which are independent of the structural model. Patterson maps show a negative peak at about 1 Å from the origin, in agreement with water being crystallized in the structure. Fourier analyses of the NPD patterns with the structure found by X-rays showed two negative peaks (b_H = −3.74 fm) near the 4c Wyckoff position with y = 0.31 that must correspond to H nuclei. This drove us to conclude that water molecules are placed at this position.

This model rendered a good refinement of synchrotron XRPD (R_B = 4.25%, χ^2 = 3.2) data. Refinement of the NPD data renders worse agreement parameters due to two facts: the larger preferred orientation owing to the large amount of material needed to fill the sample holder (≈8 mm in diameter), which is not rotated during data collection, and, most important, the large incoherent scattering introduced by hydrogen atoms in the NPD patterns. Since the values obtained for the Debye−Waller factors are strongly dependent on the absorption correction considered, we have considered U of Mo to be the same for SXRPD and NPD to indirectly estimate absorption effects. Agreement factors improve significantly considering anisotropic Debye−Waller factors (R_B = 6.3%, χ^2 = 3.4).

Even if agreement factors derived from the above-mentioned refinements are proof of the reliability of the structural model proposed, a few tiny peaks remain unindexed, with integrated intensities <1% compared to the most intense peak for both SXRPD and NPD. Such reflections can be indexed by doubling the a parameter in the $Pbca$ space group (a = 7.1894(2), b = 21.2461(1), and c = 7.3893(2) Å). Since the peaks are clearly seen in the SXRPD, we could hypothesize that the superstructure is related to a small displacement in the position of the heavier atoms. A plausible hypothesis, in agreement with the larger B values obtained for Mn than for Mo (3.7 and 1.6, respectively), is that the superstructure originates from slight

dx.doi.org/10.1021/ic401447p | Inorg. Chem. 2013, 52, 9791−9797

distortions within the MnX_6 octahedra. An electron diffraction study was undertaken with the aim of showing further light on that matter. The sample was rather stable upon irradiation, and so the reconstruction of the reciprocal lattice was possible. Yet, interpretation of the results is tricky due to double diffraction and to the very thin nature of the crystals along the *b*-direction. This, coupled to the long value *b* parameter (b = 21.2 Å), leads to elongated diffraction rods from upper levels penetrating the diffraction sphere.[34] Figure 3 exhibits a representative image of

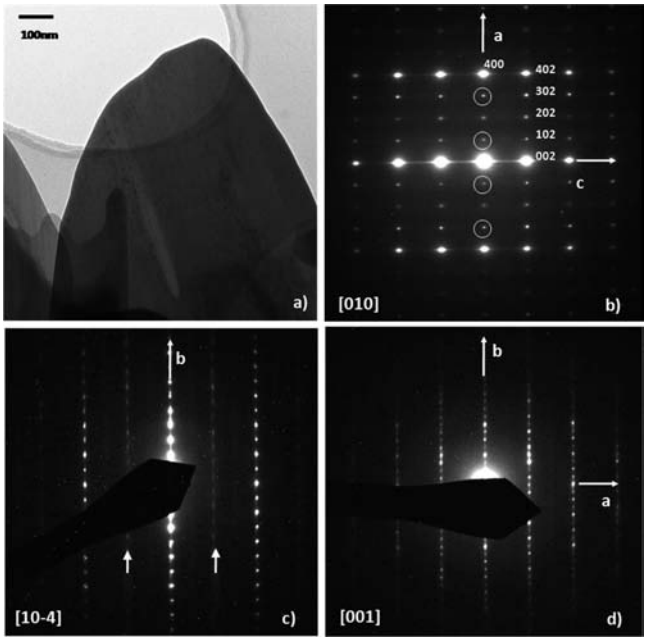

Figure 3. (a) Typical TEM image for $NaMnMoO_3F_3{\cdot}H_2O$ and electron diffraction patterns corresponding to the (b) [010], (c) [10−4], and (d) [001] zone axis. The circles marked in (b) correspond to double diffraction spots, and the white arrows in (c) indicate diffuse extra lines at positions between the 0*k*0 and *h*0*l* reflections.

a crystallite together with electron diffraction patterns for the [001] and [010] zone axes. Taking into account the above-mentioned issues, patterns were indexed with the *C*-*c*-extinction symbol and cell parameters of a = 3.60, b = 20.93, and c = 7.46 Å (Figure 4. Still, additional unindexed reflections were observed in all crystals at (1/2 *kl*) and (3/2 *kl*) (see Figure 3b) in agreement with the above-mentioned doubling of the *a* parameter. The indexing considering such reflections unambiguously points to the *Pbca* space group. Also, most crystals exhibited very weak additional spots or diffuse lines (Figure 3c), which would be consistent with the doubling of the *b* and *c* parameters, pointing to an even larger unit cell and a more complex superstructure.

The crystal structure of $NaMnMoO_3F_3{\cdot}H_2O$ is depicted in Figure 5. It is formed by the stacking along the *b*-axis of layers of MnX_6 octahedra (purple octahedra, X = O, F) that share corners along *c*- and *a*-directions. These MnX_6 layers are connected to MoX_6 (olive green) octahedra, while Na ions (yellow) and water molecules are accommodated in the large interlayer space.

Elucidation of F/O ordering was attempted by applying Pauling's second crystal rule.[4,35] The bond strength sums (b) for each anionic position (X1−X4) were calculated as 1.78, 0.92, 1.12, and 2, respectively, which would point to X1 and X4 being occupied by O and both X2 and X3 by F. The

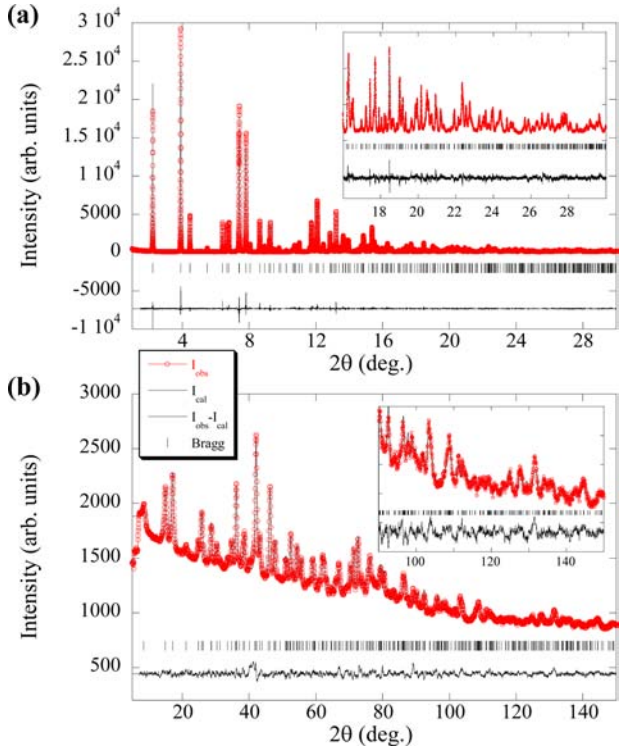

Figure 4. (a) Synchrotron XRPD and (b) NPD patterns (small circles) showing the final Rietveld fit (solid line) with the difference pattern below. Insets depict an expanded view of the high-angle region.

multiplicities of these positions for full occupation are in agreement with the proposed formula unit. Such distribution seems chemically reasonable in the sense that X1(O) is a corner bridging position between three MX_6 octahedra (two MnX_6 and a MoX_6) and X3(F) is a terminal corner position for a MoX_6 octahedron. The other remaining positions, X2 and X4, are both corner bridging between two MX_6 octahedra, with M = Mn for X2(F) and M = Mo for X4(O). Results are also consistent with the more highly charged anion being coordinated to the cation with the higher oxidation state.

In order to confirm the above-mentioned conclusions, we performed a bond valence sum (BVS) analysis (using parameters implemented in FullPof_Suite of programs) exploring all the cationic distributions compatible with the stoichiometry: (i) X1,X4 = O and X2,X3 = F; (ii) X1,X4 = F and X2,X3 = O; or (iii) X1 = O; X2,X4 = F, and X3 = O/F. Similar BVS values were obtained in all cases for manganese and sodium (close to 2.0 and 1.0, respectively), while significant differences were observed for molybdenum. The anionic distribution deduced from Pauling's second rule (i) renders a value of 5.9, while (ii) and (iii) yielded, respectively, 5.5 and 6.4; these values are either not consistent with the results of magnetic measurements or unrealistic.

Cell parameters and atomic positions for the average cell, considering the O/F ordering scheme, are given in Table 1, while selected bond distances and angles are reported in Table 2.

The presence of sodium ions in the structure does certainly contribute to ordering of anions. Indeed, all inorganic solids composed of long-range ordered oxide fluoride transition metal anions contain sodium cations.[36] The coordination environment around sodium ions can be described as a distorted cube with the two shortest Na−F2 (2.330(3) Å) and two longest

dx.doi.org/10.1021/ic401447p | Inorg. Chem. 2013, 52, 9791−9797

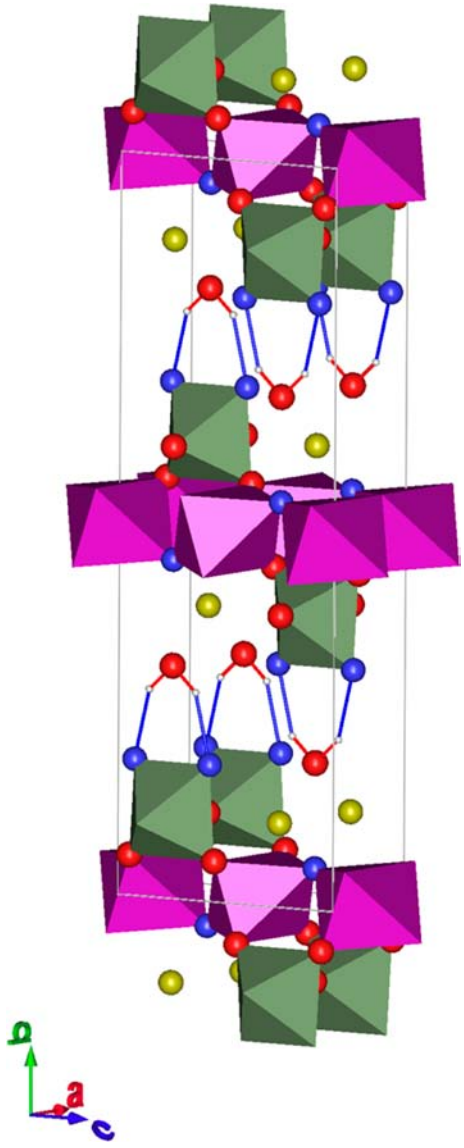

Figure 5. Crystal structure for $NaMnMoO_3F_3 \cdot H_2O$ Mn−X octahedra (purple) and Mo−X (olive green). Yellow spheres represent sodium ions.

Na−F3 (2.864(4) Å) distances. These values compare well with Na−F distances observed for the Na1 cubic in Na_2MnMF_7 (M = Cr, V) weberites[37,38] that range from 2.27 to 2.49 Å. Similar Na−F distances around 2.3 Å are also reported for layered $NaNbO_2F_2$,[39] which exhibits 6 + 1 coordination around sodium with Na−O distances of 2.58 and 3.13 Å. The Na−O distances for $NaMnMoO_3F_3 \cdot H_2O$ are 2.579(3) for O1 and 2.386(3) Å for Ow. For comparison, Na−O and Na−Ow distances around 2.33 Å have been reported for six-coordinated sodium ions in $NaMoO_3F$[40] and $Rb_3Na(MO_2F_4)_2 \cdot H_2O$ (M = Mo, W),[36] respectively.

The water molecule performs a dual role in the structure coordinating sodium and enlarging the interlayer distance so that electrostatic repulsion between the layers is lowered. The H−O distance is 0.96(7) Å and H−O−H bonding angle is 101(5)°, which would indicate a possible hydrogen bonding between H and F(X3). Distances are 2.09 Å for H−F3 (drawn with blue lines in Figure 5) and 2.54 Å for H−F3 in the plane.

Table 1. Structural Details Found by the Joint Rietveld Refinement of NPD and Synchrotron XRPD Data[a]

a (Å)		3.5947(1)
b (Å)		21.246(1)
c (Å)		7.3893(2)
Na	*y*	0.885(1)
Mo	*y*	0.135(1)
O_W	*y*	0.312(1)
X2	*y*	0.455(1)
X4	*y*	0.605(1)
H	*y*	0.282(2)
	z	0.354(4)
X1	*y*	0.056(4)
	z	0.445(1)
X3	*y*	0.188(1)
	z	0.425(1)

[a]The space group that was used is *Cmcm*. Mn is located at 4*b* (0 1/2 0) Wyckoff positions; Mo, Na, O_W, X2, and X4 are located at 4*c* (0 *y* 1/4) Wyckoff positions; and H, X1, and X3 at 8*f* (0 *y z*) positions.

Table 2. Selected Bond Lengths and Angles Resulting from the Joint Rietveld Refinement of NPD and Synchrotron XRPD Data

	length (Å)		angle (deg)
Mn			
d_{Mn-O1}	2.192(5)	O1−Mn−O1 (x2)	110.2(2)
		O1−Mn−O1 (x2)	69.8(4)
		O1−Mn−O1 (x2)	180.00(-)
d_{Mn-F2}	2.078(6)	O1−Mn−F2 (x4)	94.7(4)
		O1−Mn−F2 (x4)	85.3(3)
		F2−Mn−F2	180.00(-)
Mo			
d_{Mo-O1}	2.207(6)	O1−Mo−O1	81.4(5)
		O1−Mo−O4 (x4)	75.5(4)
		O1−Mo−F3 (x2)	90.6(9)
		O1−Mo−F3 (x2)	172.0(9)
d_{Mo-O4}	1.905(9)	O4−Mo−O4	141.4(2)
		O4−Mo−F3 (x4)	102.6(6)
d_{Mo-F3}	1.716(9)	F3−Mo−F3	97.3(9)

The distribution of anions yields distorted octahedral MO_4F_2 (M = Mo, Mn) units for both transition metals (see values in Table 2 and a scheme depicting coordination environments in Figure 6). Distorted MX_6 coordination has been reported for O/F anion ordered structures, consisting of either discrete[30−32,41] or connected Mo(VI)X_6 octahedra.[40,42−44] $NaMoO_3F_3$ elpasolites,[31,32] exhibiting discrete Mo(VI)X_6 octahedra, and other compounds with bioctahedral corner-sharing[42] $(Mo_2O_5F_6)^{4-}$ or face-sharing[43] $(Mo_2O_6F_3)^{3-}$ units tend to show three longer and three shorter Mo−X distances. Structures with higher connectivity (i.e., a larger number of bridging anions) have been shown to exhibit alternative distortions. $MnMoO_4$, with a corner-sharing M(VI)O_6 three-dimensional structure,[45] exhibits two short, two medium, and two long M−O distances around 1.7, 1.9, and 2.1 Å, respectively, as is also the case for MoO_2F_2,[44] with a triangular columnar framework, and $NaMoO_3F$,[40] which is built of edge-sharing Mo(VI)X_6 octahedra double chains. In the case of $NaMnMoO_3F_3 \cdot H_2O$, distances around Mo (VI) are similar to the latter: Mo−O1 = 2.207(6), Mo−F3 = 1.716(9), and Mo−

dx.doi.org/10.1021/ic401447p | Inorg. Chem. 2013, 52, 9791−9797

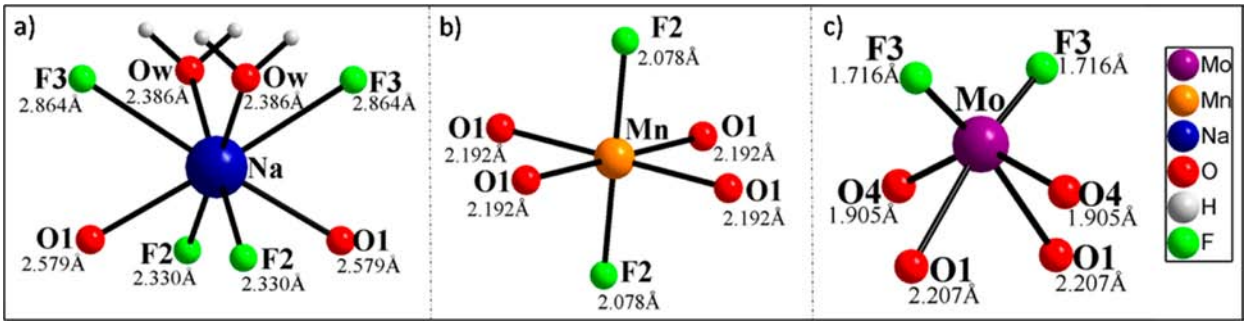

Figure 6. Scheme depicting coordination environments around metal atoms.

F4 = 1.905(9) Å. The shortest Mo−F3 distances correspond to terminal anions in *cis*-configuration in full agreement with observations for $NaMoO_3F$.[40]

$Mn(II)X_6$ octahedra are all corner-sharing, with the coordination around Mn exhibiting four Mn−O1 2.192(5) Å "equatorial" and two Mn−F2 2.078(6) Å "axial" distances (see Table 2 and Figure 6). Such values compare well with those reported in the literature for corner-sharing $Mn(II)O_6$ (e.g., 2.08−2.30 Å for $MnMoO_4$[45] and $Mn(II)F_6$ and 2.04−2.09 Å for $NaMnF_3$[46] and Na_2MnMF_7 weberites).[37,38] While the F2−Mn−F2 angle is 180°, the refinement yields bond angle values in the Mn−O1 "equatorial", which depart significantly from 90° (69.8° and 110.1°); this could be an indication that the coordination around manganese atoms is not well-represented by the average structure, and a plausible splitting of manganese positions is at the origin of the observed superstructure.

Electrochemical tests in tight cells against sodium counter electrodes were carried out, and the compound was found to deliver a capacity close to 600 mAh/g upon reduction at an average potential of 0.5V vs Na^+/Na^0 of which only 25% was reversible, indicating that even if the existence of a conversion reaction[9] is plausible, electrolyte decomposition is the major process taking place.[48] Additionally, the possibility of sodium extraction with concomitant oxidation of $NaMnMoO_3F_3{\cdot}H_2O$ was also checked. Preliminary results indicated that oxidation was indeed possible at ≈4.4 V vs Na^+/Na^0 and partially reversible (see Figure S2 from the SI, including a full oxidation/reduction cycle) in a electrochemical cell using sodium metal counter electrodes. In operando X-ray diffraction was performed during the full cycle using a homemade cell with a Be window[47] and did not reveal any modification in the pattern of the pristine $NaMnMoO_3F_3{\cdot}H_2O$ (see Figure S3). Such results do clearly prove that the redox processes observed are unfortunately not related to sodium deinsertion and reinsertion in the material, but rather they are due to electrolyte degradation. Indeed, the well-known catalytic activity of transition metals with respect to reactions involving organic compounds can induce parasitic electrolyte decomposition at a lower potential than that observed with inert metal electrodes.[49] Such results highlight the need to use supplementary characterization techniques, as in operando diffraction, to confirm electrochemical activity in new compounds because electrochemical testing alone can be misleading. The electrochemical activity of $NaMnMoO_3F_3{\cdot}H_2O$ cannot be fully excluded by the above-mentioned results, but if any activity occurs, it would take place at potentials that cannot be achieved with standard electrolytes. This is also a major hurdle for the development of high-potential Li-ion batteries, and we are confident that future breakthroughs in that area will lead to new concepts that could enable further development of such "reactive" mixed transition metal compounds.

CONCLUSIONS

The synthesis and characterization of $NaMnMoO_3F_3{\cdot}H_2O$ is reported. It was prepared through precipitation at low temperature, and its crystal structure has been elucidated through powder diffraction methods (synchrotron and neutron). The average crystal structure exhibits a = 3.596, b = 21.247, and c = 7.389 Å cell parameters and *Cmcm* (No. 63) space group, but tiny superstructure peaks are observed, which can be indexed with space group *Pbca* and cell parameters a =7.18294(2), b = 21.246(1), and c = 7.3893(2) Å. The electron diffraction study confirms the doubling of the a parameter, and indexing is consistent with the *Pbca* space group. However, the existence of very weak additional spots or diffuse lines points to an even larger unit cell and a more complex superstructure, which could not be fully elucidated. The structure can be described as a stacking along the b-axis of MnX_6 octahedra layers that share corners along c- and a-directions. MoX_6 octahedra connected to the layer are sitting in the interlayer space together with sodium ions and water molecules. F/O ordering is proposed with X1 and X4 being occupied by O and X2 and X3 by F, which is in full agreement with multiplicities and chemical formula. Such a distribution is consistent with the more highly charged anion being coordinated to the cation with higher oxidation state, which is chemically expectable. Sodium ions exhibit a distorted cubic environment being coordinated to water molecules. The distribution of anions yield distorted octahedral MO_4F_2 (M = Mo, Mn) units for both transition metals. For MoO_4F_2, bond distances range from 1.71 to 2.2 Å, the shortest values corresponding to terminal F anions in *cis*-configuration. MnO_4F_2 octahedra are all corner sharing, with the coordination around Mn exhibiting four Mn−O1 2.19 Å "equatorial" and two Mn−F2 2.08 Å "axial" distances, with bond angles significantly departing from the expected values, which indicates that the coordination around manganese ions is not well-represented by the average structure and could be at the origin of the observed superstructure. The feasibility of electrochemically extracting sodium upon reduction in cells using sodium counter electrodes was prevented by electrolyte decomposition. Yet, such a layered structure may be prone to sodium ion diffusion and reversible extraction of sodium at higher potentials cannot be excluded.

ASSOCIATED CONTENT

Supporting Information

CIF file, typical XRD for pristine NaMnMoO3F3·H2O, electrochemical data, and in operando XRD patterns. This

dx.doi.org/10.1021/ic401447p | *Inorg. Chem.* 2013, 52, 9791−9797

material is available free of charge via the Internet at http://pubs.acs.org.

AUTHOR INFORMATION

Corresponding Author

*E-mail: rosa.palacin@icmab.es.

Notes

The authors declare no competing financial interest.

ACKNOWLEDGMENTS

We acknowledge the Ministerio de Ciencia e Innovación (Spain) for Grant MAT2011-24757 and ALISTORE-ERI members for fruitful discussions. We also thank Lynn Ribaud for assistance in collecting data at the 11-BM line at Argonne National Laboratory. The use of the Advanced Photon Source at Argonne National Laboratory was supported by the U.S. Department of Energy, Office of Science, and Office of Basic Energy Sciences under Contract No. DE-AC02-06CH11357. We are grateful for neutron diffraction beamtime, which was granted through Institut Laue Langevin's Easy Access SYstem (EASY).

REFERENCES

(1) *Inorganic Solid Fluorides: Chemistry and Physics*; Hagenmuller, P., Ed.; Academic Press: New York, 1985.
(2) Shannon, R. D. *Acta Crystallogr.* **1976**, *A32*, 751.
(3) Simon, A.; Ravez, R. *Ferroelectrics* **1980**, *24*, 305.
(4) Fuertes, A. *Inorg. Chem.* **2006**, *45*, 9640.
(5) Amatucci, G. G.; Pereira, N. *J. Fluorine Chem.* **2007**, *128*, 243.
(6) Barker, J.; Saidi, M. Y.; Swoyer, J. L. *J. Electrochem. Soc.* **2003**, *150*, A1394.
(7) Recham, N.; Chotard, J. N.; Dupont, L.; Delacourt, C.; Walker, W.; Armand, M.; Tarascon, J. M. *Nat. Mater.* **2010**, *9*, 68.
(8) Bervas, M.; Klein, L. C.; Amatucci, G. G. *J. Electrochem. Soc.* **2006**, *153*, A159.
(9) Cabana, J.; Monconduit, L.; Larcher, D.; Palacin, M. R. *Adv. Mater.* **2010**, *12*, 315.
(10) Pereira, N.; Badway, F.; Wartelsky, M.; Gunn, S.; Amatucci, G. G. *J. Electrochem. Soc.* **2009**, *156*, A407.
(11) Gonzalo, E.; Kuhn, A.; Garcia-Alvarado, F. *J. Power Sources* **2010**, *195*, 4990.
(12) Bassa, A.; Gonzalo, E.; Kuhn, A.; Garcia-Alvarado, F. *J. Power Sources* **2012**, *207*, 160.
(13) Nishijima, M.; Gocheva, I. D.; Okada, S.; Doi, T.; Yamaki, J. I.; Nishida, T. *J. Power Sources* **2009**, *190*, 558.
(14) Kitajou, A.; Komatsu, H.; Chihara, K.; Gocheva, I. D.; Okada, S.; Yamaki, J. I. *J. Power Sources* **2012**, *198*, 389.
(15) Sorensen, E. M.; Izumi, H. K.; Vaughey, J. T.; Stern, C. L.; Poeppelmeier, K. R. *J. Am. Chem. Soc.* **2005**, *127*, 6347.
(16) Sauvage, F.; Bodenez, V.; Vezin, H.; Albrecht, T. A.; Tarascon, J. M.; Poeppelmeier, K. R. *Inorg. Chem.* **2008**, *47*, 8464.
(17) Atuchin, V. V.; Molokeev, M. S.; Yurkin, G. Y.; Gavrilova, T. A.; Kesler, V. G.; Laptash, N. M.; Flerov, I. N.; Patrin, G. S. *J. Phys. Chem. C* **2012**, *116*, 10162.
(18) Massa, W.; Babel, D. *Chem. Rev.* **1988**, *88*, 275.
(19) Burgher, F.; Mathieu, L.; Lati, E.; Gasser, P.; Peno-Mazzarino, L.; Blomet, J.; Hall, A. H.; Maibach, H. I. *Cutaneous Ocul. Toxicol.* **2011**, *30*, 100.
(20) Burgher, F.; Mathieu, L.; Lati, E.; Gasser, P.; Peno-Mazzarino, L.; Blomet, J.; Hall, A. H.; Maibach, H. I. *Cutaneous Ocul. Toxicol.* **2011**, *30*, 108.
(21) Hewat, A. *Physica B* **2006**, *385*−*386*, 979.
(22) Boultif, A.; Louer, D. *J. Appl. Crystallogr.* **2004**, *37*, 724.
(23) Rius, J.; Vallcorba, O.; Peral, I.; Frontera, C.; Miravitlles, C. *J. Appl. Crystallogr.* **2012**, *45*, 844.
(24) Rius, J. *Acta Crystallogr., Sect. A* **2011**, *67*, 63.
(25) Rodríguez-Carvajal, J. *Physica B* **1993**, *192*, 55.
(26) Nakamoto, K. *Infrared and Raman Spectra of Inorganic and Coordination Compounds: Part A—Theory and Applications in Inorganic Chemistry*, 6th ed.; John Wiley & Sons: Hoboken, NJ, 2009.
(27) Vimont, A.; Lavalley, J. C.; Fracke, L.; Demourgues, A.; Tressaud, A.; Daturi, M. *J. Phys. Chem. B* **2004**, *108*, 3426.
(28) Demourgues, A.; Penin, N.; Dambournet, D.; Clarenc, R.; Tressaud, A.; Durand, E. *J. Fluorine Chem.* **2012**, *134*, 35.
(29) Sheng, J.; Tang, K.; Cheng, W.; Wang, J.; Nie, Y.; Yang, Q. *J. Hazard. Mater.* **2009**, *171*, 279.
(30) Aldous, D.; Lightfoot, P. *Solid State Sci.* **2009**, *11*, 315.
(31) Brink, F.; Norén, L.; Goossens, D.; Withers, R.; Liu, Y.; Xu, C. *J. Solid State Chem.* **2003**, *174*, 450.
(32) Maggard, P.; Nault, T.; Stern, C.; Poeppelmeier, K. *J. Solid State Chem.* **2003**, *175*, 27.
(33) Fry, A.; Seibel, H., II; Lokuhewa, I.; Woodward, M. P. *J. Am. Chem. Soc.* **2012**, *134*, 2621.
(34) Ross, M.; Christ, C. L. *Am. Mineral.* **1958**, *43*, 1157.
(35) Pauling, L. *J. Am. Chem. Soc.* **1929**, *51*, 1010.
(36) Marvel, M. R.; Pinlac, R. A. F.; Lesage, J.; Stern, C.; Poeppelmeier, K. R. *Z. Anorg. Allg. Chem.* **2009**, *635*, 869.
(37) Peschel, B.; Babel, D. *Z. Anorg. Allg. Chem.* **1997**, *623*, 1614.
(38) Courbion, G.; Ferey, G.; Holler, H.; Babel, D. *Eur. J. Solid State Inorg. Chem.* **1988**, *25*, 435.
(39) Anderson, S.; Galy, J. *Acta Crystallogr.* **1969**, *B25*, 847.
(40) Moutou, J.-M.; Chaminade, J.-P.; Pouchard, M.; Hagenmuller, P. *Rev. Chim. Miner.* **1986**, *23*, 27.
(41) Chamberlain, K.; Albrecth, T.; Lesage, J.; Sauvage, F.; Stern, C.; Poeppelmeier, K. R. *Cryst. Growth Des.* **2010**, *10*, 4868.
(42) Fourquet, J. L.; Duroy, H.; Crosnier-Lopez, M. P. *Z. Anorg. Allg. Chem.* **1997**, *623*, 439.
(43) Kirsch, J. E.; Izumi, H. K.; Stern, C. L.; Poeppelmeier, K. R. *Inorg. Chem.* **2005**, *44*, 4586.
(44) Shorafa, H.; Ficicioglu, H.; Tamadon, F.; Girgsdies, F.; Seppelt, K. *Inorg. Chem.* **2010**, *49*, 4263.
(45) Clearfield, A.; Moini, A.; Rudolf, P. R. *Inorg. Chem.* **1985**, *24*, 4606.
(46) Ratuszna, A.; Majewska, K. *Acta Crystallogr., Sect. C* **1989**, *45*, 548.
(47) Morcrette, M.; Chabre, Y.; Vaughan, G.; Amatucci, G.; Leriche, J.-B.; Patoux, S.; Masquelier, C.; Tarascon, J.-M. *Electrochim. Acta* **2002**, *47*, 3137.
(48) Ponrouch, A.; Taberna, P.L.; Simon, P.; Palacín, M.R. *Electrochim. Acta* **2012**, *61*, 13.
(49) Ponrouch, A.; Marchante, E.; Courty, M.; Tarascon, J.-M.; Palacín, M. R. *Energy Environ. Sci.* **2012**, *5*, 8572.